ChemComm

COMMUNICATION

View Article Online
View Journal



Cite this: DOI: 10.1039/c6cc00520a

Received 19th January 2016,
Accepted 29th February 2016

DOI: 10.1039/c6cc00520a

www.rsc.org/chemcomm

# Mesoporous and carbon hybrid structures from layered molecular precursors for Li-ion battery application: the case of β-$In_2S_3$†

Ming-Jian Zhang,‡ Lei-Lei Tian,‡ Shuankui Li, Ling-Piao Lin and Feng Pan*

**A new method was demonstrated to construct mesoporous and carbon hybrid structures of β-$In_2S_3$ from the thermal decomposition of layered molecular precursors. When applied to LIBs, they all exhibit good cycling stability and excellent rate performance due to the great uniformity of mesopores and pyrolysis carbon distributed in the materials.**

The performance of lithium ion batteries (LIBs) greatly depends on the performance of the electrode materials.[1–3] High reversible capacity, excellent cycling stability and good rate performance are three basic requirements for the electrode materials.[4] As for the anode materials, the typical intercalation material graphite exhibits a good cycling stability but a low specific capacity (372 mA h $g^{-1}$) and a poor rate capability. So a wide variety of alloy- and conversion-type materials with very high theoretical capacities were developed, such as Si (4200 mA h $g^{-1}$),[5–7] Ge (1600 mA h $g^{-1}$),[8] $Fe_2O_3$ (1007 mA h $g^{-1}$),[9–11] and $MoS_2$ (669 mA h $g^{-1}$),[12–14] *etc.* However, compared with intercalation materials, these materials always suffer from the serious problem of poor cycling stability, which greatly hampers their commercial application. This problem is believed to be caused by the large volume change of electrode materials during the charge–discharge cycling. These large volume changes always result in the pulverization of electrode materials and a large loss of effective electrical contact between active materials, leading to rapid capacity decay. A lot of efforts have been devoted to mitigate the great volume changes for solving the problem of poor cycling stability. Two of the most common techniques are to construct the porous structure and the carbon-based matrix structure.[15] Taking β-$In_2S_3$ ($Fd\bar{3}m$) as an example, it has a typical defect spinel structure with a lot of vacancies.[16] Both conversion and alloy reactions occur in the charge–discharge process.[17] It has a high theoretical capacity of 1206 mA h $g^{-1}$ according to the conversion-alloy reaction ($In_2S_3 + 6Li^+ + 6e^- \rightarrow 2In + 3Li_2S$; $In + 4.33Li^+ + 4.33e^- \rightarrow Li_{4.33}In$), which is three times more than that of commercial graphite.[18] However, it presented a very low capacity retention of 5.6% in the previous report.[19] So various methods, like mesoporous microsphere and carbon coating,[20] graphene composites,[21,22] and nanosheets,[18] have been adopted to improve its cycling stability. Nevertheless, its lithium storage performance still leaves much to be desired.

In this work, we demonstrate a new effective strategy, the thermal decomposition of layered molecular precursors, to obtain mesoporous structure and carbon hybrid structure for high-performance electrode materials. Taking β-$In_2S_3$ as the model material, we prepared its carbon-free and carbon-coating precursors ($NH_4InS_2$ and $EnInS_2$), respectively. By their thermal decomposition, the mesoporous structures (denoted as MIS) and carbon hybrid structures (denoted as IS/C) of β-$In_2S_3$ were obtained, respectively. Both of them exhibited good cycling performance with large capacities and excellent rate performance in comparison with commercial β-$In_2S_3$.

The molecular precursors were synthesized by the solvothermal method. Ammonia and ethylene diamine (En) were used as the solvent for the carbon-free and carbon-containing precursors, respectively. Colorless and light yellow crystals were obtained, respectively. Their crystal structures are determined by single crystal X-ray diffraction (Fig. 1). Their detailed crystal data are listed in Table S1 (ESI†), and their bond lengths and bond angles are listed in Table S2 and S3 (ESI†), respectively. The carbon-free and carbon-containing precursors crystallize in the monoclinic space group ($C2/c$) and the tetragonal space group ($I4_1/amd$), respectively. Their formulae could be derived as $NH_4InS_2$ and $EnInS_2$, respectively, according to the used solvents and the EDX results (Table S4, ESI†). As shown in Fig. 1a, the asymmetric unit of $NH_4InS_2$ is composed of four $InS_4$ tetrahedra by sharing corners. It extends into an $InS_2^-$ layer along the ab plane. Viewing from the *b* axis direction, it shows a two dimensional layered structure stacked along the *c* axis direction. There are two layers in a unit cell. The layer thickness is 5.86 Å and the interlayer spacing is 1.78 Å. $NH_4^+$ could locate between the $InS_2^-$ layers as the

*School of Advanced Materials, Peking University Shenzhen Graduate School, Shenzhen 518055, China. E-mail: panfeng@pkusz.edu.cn*

† Electronic supplementary information (ESI) available: Experiments, figures, tables, and crystallographic data in CIF. ICSD 430730 and 430731. See DOI: 10.1039/c6cc00520a

‡ Ming-Jian Zhang and Lei-Lei Tian contributed equally.

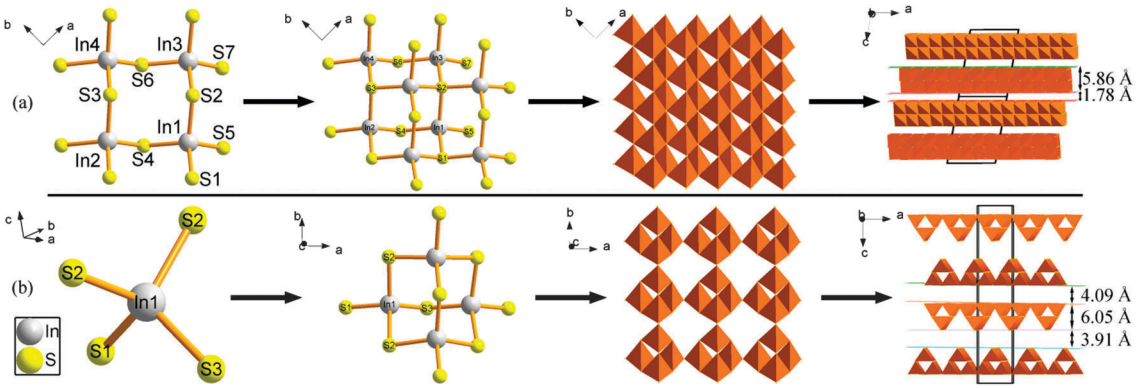


Fig. 1 The crystal structures of the layered carbon-free precursor $NH_4InS_2$ (a) and the layered carbon-containing precursor $EnInS_2$ (b). The brown tetrahedra mean $InS_4$ tetrahedra.

charge-balance cation. As shown in Fig. 1b, the asymmetric unit of $EnInS_2$ is an $InS_4$ tetrahedron. It shares corners to form an $In_4S_6$ T2 tetrahedron.[23] Similarly, these T2 tetrahedra also extend into an $InS_2^-$ layer by corner-sharing along the ab plane. Its two dimensional layered structure aligned along the *c* axis direction is also presented. Different from $NH_4InS_2$, there are four layers in a unit cell. The thickness of a single layer is 6.05 Å, and the distances between layers are 4.09 and 3.91 Å, respectively. The protonated En ($En^+$) could locate between the $InS_2^-$ layers to balance the charge. However, the exact locations of $NH_4^+$ and $En^+$ cations in their structures could not be determined, even though several single crystals have been collected. This might be due to the disorder distribution of $NH_4^+$ and $En^+$ cations between the layers. Their powder X-ray diffraction (PXRD) patterns are consistent with the simulated PXRD patterns based on the single crystal structures, proving their phase purity (Fig. S1, ESI†). The thermogravimetric (TG) analysis was performed (Fig. S2, ESI†), and the varied temperature powder XRD patterns were also measured (Fig. S3 and S4, ESI†).

Accordingly, the MIS and IS/C samples were obtained by the thermal decomposition of the carbon-free and carbon-containing precursors at 400 °C for 1 h in an Ar atmosphere (see Experimental section in the ESI†). Their morphology was investigated by SEM and TEM images (Fig. 2 and 3). As shown in Fig. 2a, the carbon-free $NH_4InS_2$ exists as a thick plate with a thickness of about 100 nm, which is consistent with its layered crystal structure. After calcination, the morphology of the thick plate was still observed, while the relatively uniformly-distributed mesopores were formed in these thick plates because of the release of $NH_3$ and $H_2S$ (Fig. 2b and c). The size of these mesopores could be estimated to be in the range of 10–20 nm from Fig. 2d. The lattice planes (220) and (300) of β-$In_2S_3$ were also observed (Fig. 2d). Similarly, $EnInS_2$ crystallized in a larger and thicker plate as shown in Fig. 3a. The thickness of these plates was about 1 μm. After the calcination process, the macroscopical morphology of the thick plate was also preserved as shown in Fig. 3b and c. These thick plates were constructed using a lot of closely-stacked thin plates, and many irregular interstices emerge between these thin plates because of the decomposition of interlayer En molecules. The lattice plane (400) of β-$In_2S_3$ was

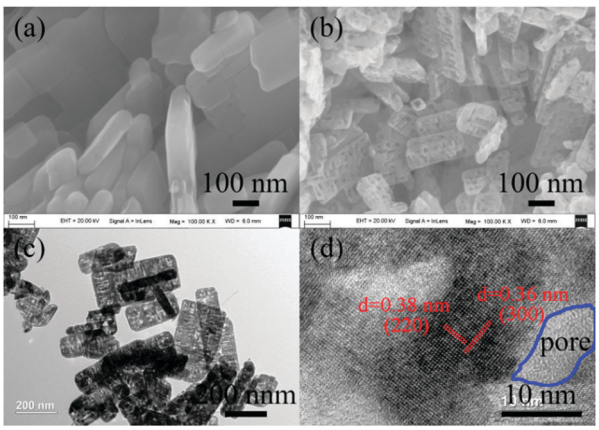


Fig. 2 SEM images of the carbon-free precursor $NH_4InS_2$ (a) and the MIS sample (b); TEM (c) and HRTEM (d) images of the MIS sample.

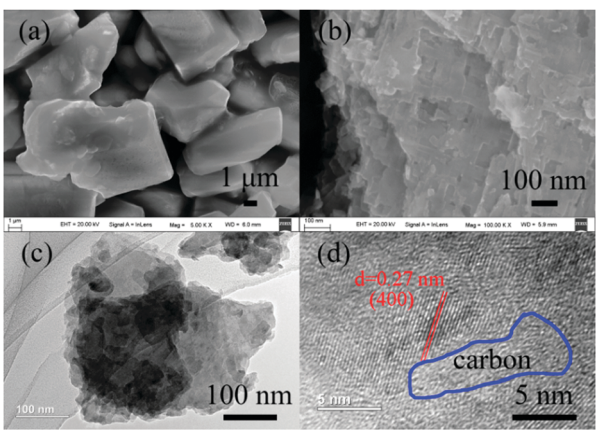


Fig. 3 SEM images of the carbon-containing precursor $EnInS_2$ (a) and the IS/C sample (b); TEM (c) and HRTEM (d) images of the IS/C sample.

observed in the thin plate (Fig. 3d). The domains without lattice fringes might be assigned to the pyrolysis carbon. So these thin plates can be identified as carbon hybrid β-$In_2S_3$ with a great uniformity at the nanometer level. In order to further confirm the chemical composition of the IS/C sample, EDX mapping was performed using TEM. As shown in Fig. S5 (ESI†), three elements,

 

In, S and C, are uniformly distributed on these thin plates, which might be caused by the damage effect of the electron beam. Combining with the PXRD pattern at 400 °C (Fig. S4, ESI†), we could conclude that the thick plate was composed of the closely-stacked carbon hybrid β-$In_2S_3$ thin plate. Consequently, we could summarize the whole thermal decomposition process in a schematic diagram (Fig. S9, ESI†). The carbon-free and carbon-containing layered precursors decomposed into mesoporous structure and carbon hybrid structure, respectively. It could be predicted that these relatively uniformly-distributed mesopores and pyrolysis carbon can effectively buffer the volume change during the lithiation and delithiation cycles, and contribute to a good electrode performance in the LIBs.

The $N_2$ adsorption–desorption measurements were performed to further characterize the porosity of MIS and IS/C (Fig. S6, ESI†). They both exhibit a type III $N_2$ adsorption–desorption isotherm, which is a typical characteristic of mesoporous materials. For the MIS sample, the pore size is mainly located in the range of 10–30 nm (inset in Fig. S6a, ESI†), which is consistent with the SEM and TEM images of the MIS sample (Fig. 2b–d), while there is a relatively dispersive distribution of the pore size for the IS/C sample (inset in Fig. S6b, ESI†), which might correspond to the interstices between the thin plates (Fig. 3b). The Brunauer–Emmett–Teller (BET) specific surface areas were calculated as 46.13 and 16.37 $m^2\ g^{-1}$ for MIS and IS/C, respectively. The Raman spectrum is also recorded to get insight into the phase composition of the pyrolysis carbon in the IS/C sample (Fig. S8, ESI†). A small peak at about 300 $cm^{-1}$ could be assigned to $In_2S_3$.[24] Two main peaks at around 1385 $cm^{-1}$ and 1583 $cm^{-1}$ correspond to the D and G bands of pyrolysis carbon, respectively. The intensity ratio of D/G is about 1.9, which demonstrates the presence of the $sp^2$ domains and a good crystallization of pyrolysis carbon.

Finally, the MIS and IS/C samples were fabricated into the anodes of LIBs to test their electrode performance (see Experimental section in the ESI†). Commercial $In_2S_3$ (denoted as IS) was bought for comparison. Fig. 4a shows the cycling performance of IS, MIS and IS/C at a current density of 0.1 A $g^{-1}$. It is obvious that MIS and IS/C show significantly improved capacities and cycling stability than IS. MIS shows initial discharge and charge capacities of 1921 and 785 mA h $g^{-1}$, while those of IS/C are 1133 and 787 mA h $g^{-1}$. The coulombic efficiencies for the IS, MIS and IS/C samples in the first cycle were calculated to be 61.7%, 40.9%, and 69.5%, respectively. The first cycle capacity losses could be ascribed to the irreversible loss of Li ions caused by the formation of SEI films and the irreversible reactions from In to $In_2S_3$ in the charge process. In Fig. 4a, the stable capacity of IS/C is about 300 mA h $g^{-1}$ larger than that of MIS, which could be attributed to the following cause. The pyrolysis carbon in IS/C uniformly divides the thin plates into much smaller regions (Fig. 3d), which greatly increase the effective electrochemically active surface. The charge capacity was stabilized at about 750 mA h $g^{-1}$ after just 5 cycles for IS/C, while it was stabilized at about 500 mA h $g^{-1}$ after 20 cycles for MIS. It demonstrates that the stable solid electrolyte interphase (SEI) film was constructed more swiftly in IS/C than in MIS. It could be ascribed to the uniform carbon hybrid in IS/C and the larger

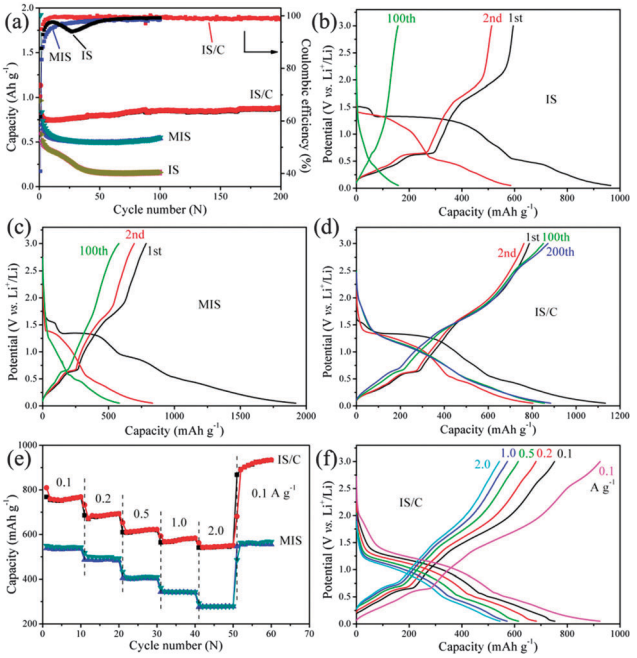


Fig. 4 (a) Cycling performance at current density of 0.1 A $g^{-1}$; galvanostatic charge–discharge profiles for the IS (b), MIS (c) and IS/C (d) samples at 0.1 A $g^{-1}$; (e) rate performance at various current densities; (f) galvanostatic charge–discharge profiles of IS/C at various current densities. The 5th cycle was selected to plot the profile at each current density.

grain size in MIS. Notably, both samples show a slight increase of capacities in the subsequent cycles. The discharge and charge capacities increase to 884 and 872 mA h $g^{-1}$ for IS/C after 200 cycles, while they rise up to 550 and 542 mA h $g^{-1}$ for MIS after 100 cycles. The lower capacity during the first few cycles might be ascribed to an active process of electrode materials, which is caused by Li ions inserted in the $In_2S_3$ framework in the initial cycles and then released gradually upon cycling.[18,20] In comparison, the discharge and charge capacities of IS in the first cycle are about 965 and 595 mA h $g^{-1}$, but with poor stability during the initial 40 cycles as previously reported.[21,22] In addition, the 1st, 2nd, 100th, and/or 200th charge–discharge plots for IS, MIS and IS/C are shown in Fig. 4b–d. Two potential plateaus in the first discharge process were observed at about 1.5 and 1.3 V (*vs.* $Li/Li^+$). They could be ascribed to the reduction reactions of $In^{3+}$ to $In^{2+}$ and $In^{2+}$ to $In^0$, respectively.[22] Their second cycles show initial capacity losses owing to the irreversible loss of Li ions caused by the formation of SEI films.[25]

The MIS and IS/C electrodes were tested at stepwise increased current densities of 0.1, 0.2, 0.5, 1.0 and 2.0 A $g^{-1}$ in Fig. 4e, and 10 cycles were performed at each current density. Before rate performance testing, the cells were activated at 0.1 A $g^{-1}$ for 20 cycles. Remarkably, the discharge and charge capacities of IS/C are both 545 mA h $g^{-1}$ at 2.0 A $g^{-1}$, much higher than that (430 mA h $g^{-1}$) of the graphene composite,[22] showing an excellent rate performance. The MIS electrode also exhibits good rate performance with specific capacity (278 mA h $g^{-1}$) at 2.0 A $g^{-1}$, about half that of IS/C. The curves also indicate that the discharge and charge capacities are very stable at the same

current density. Finally, they returned to be tested at 0.1 A $g^{-1}$ and displayed a stability during the last 10 cycles, showing an excellent rate capability of MIS and IS/C. In Fig. 4f, it is obvious that the charge–discharge profile at 2.0 A $g^{-1}$ was similar to that at 0.1 A $g^{-1}$, indicating that the electrochemical process was basically unchanged even at higher current density.

In summary, a new method was developed to construct mesoporous structures and carbon hybrid structures for high-performance electrode materials from molecular precursors. Carbon-free and carbon-containing precursors ($NH_4InS_2$ and $EnInS_2$) were decomposed into mesoporous materials and carbon hybrid materials, respectively. The uniform distribution of $NH_4^+$ and $En^+$ at the molecular level in the precursors lead to the excellent uniformity of the mesopores and the pyrolysis carbon in the samples. They both exhibit high specific capacities, and excellent cycling and rate performance. Remarkably, the carbon hybrid sample realized a very high specific capacity of 880 mA h $g^{-1}$ after 200 cycles, and a much better rate performance than the graphene composite reported before.

All these results demonstrate that the thermal decomposition of molecular precursors is a valuable approach to prepare high-performance electrode materials for LIBs.

This work was supported by the Guangdong innovative team program (2013N080), the peacock plan (KYPT20141016105435850), Shenzhen Science and Technology Research Grant (JCYJ2015 0629144526408, JCYJ20150629144453251), Chinese postdoctoral science foundation (2015M570882, 2015M570894).

## Notes and references

1 D. Larcher and J. M. Tarascon, *Nat. Chem.*, 2015, **7**, 19.
2 N. Nitta, F. Wu, J. T. Lee and G. Yushin, *Mater. Today*, 2015, **18**, 252.
3 J. Hassoun and B. Scrosati, *J. Electrochem. Soc.*, 2015, **162**, A2582.
4 L. L. Tian, X. Y. Wei, Q. C. Zhuang, C. H. Jiang, C. Wu, G. Y. Ma, X. Zhao, Z. M. Zong and S. G. Sun, *Nanoscale*, 2014, **6**, 6075.
5 H. Tian, F. Xin, X. Wang, W. He and W. Han, *J. Materiomics.*, 2015, **1**, 153.
6 U. Kasavajjula, C. Wang and A. J. Appleby, *J. Power Sources*, 2007, **163**, 1003.
7 C. K. Chan, H. Peng, G. Liu, K. McIlwrath, X. F. Zhang, R. A. Huggins and Y. Cui, *Nat. Nanotechnol.*, 2008, **3**, 31.
8 C. K. Chan, X. F. Zhang and Y. Cui, *Nano Lett.*, 2008, **8**, 307.
9 J. T. Hu, J. X. Zheng, L. L. Tian, Y. D. Duan, L. P. Lin, S. H. Cui, H. Peng, T. C. Liu, H. Guo, X. W. Wang and F. Pan, *Chem. Commun.*, 2015, **51**, 7855.
10 L. L. Tian, M. J. Zhang, C. Wu, Y. Wei, J. X. Zheng, L. P. Lin, J. Lu, K. Amine, Q. C. Zhuang and F. Pan, *ACS Appl. Mater. Interfaces*, 2015, **7**, 26284.
11 L. L. Tian, Q. C. Zhuang, J. Li, C. Wu, Y. L. Shi and S. G. Sun, *Electrochim. Acta*, 2012, **65**, 153.
12 D. Chen, G. Ji, B. Ding, Y. Ma, B. Qu, W. Chen and J. Y. Lee, *Ind. Eng. Chem. Res.*, 2014, **53**, 17901.
13 D. Kong, H. He, Q. Song, B. Wang, W. Lv, Q.-H. Yang and L. Zhi, *Energy Environ. Sci.*, 2014, **7**, 3320.
14 K. Chang, D. Geng, X. Li, J. Yang, Y. Tang, M. Cai, R. Li and X. Sun, *Adv. Energy Mater.*, 2013, **3**, 839.
15 C. Yuan, H. B. Wu, Y. Xie and X. W. Lou, *Angew. Chem., Int. Ed. Engl.*, 2014, **53**, 1488.
16 W. T. Kim and C. D. Kim, *J. Appl. Phys.*, 1986, **60**, 2631.
17 Y. Liu, H. Xu and Y. Qian, *Cryst. Growth Des.*, 2006, **6**, 1304.
18 F. Ye, C. Wang, G. Du, X. Chen, Y. Zhong and J. Z. Jiang, *J. Mater. Chem.*, 2011, **21**, 17063.
19 L. Liu, H. Liu, H.-Z. Kou, Y. Wang, Z. Zhou, M. Ren, M. Ge and X. He, *Cryst. Growth Des.*, 2009, **9**, 113.
20 G. Li and H. Liu, *J. Mater. Chem.*, 2011, **21**, 18398.
21 J. Choi, J. Jin, J. Lee, J. H. Park, H. J. Kim, D.-H. Oh, J. R. Ahn and S. U. Son, *J. Mater. Chem.*, 2012, **22**, 11107.
22 X. Yang, C. Y. Chan, H. T. Xue, J. Xu, Y.-B. Tang, Q. Wang, T. L. Wong and C.-S. Lee, *CrystEngComm*, 2013, **15**, 6578.
23 P. Y. Feng, X. H. Bu and N. F. Zheng, *Acc. Chem. Res.*, 2005, **38**, 293.
24 A. Datta, S. K. Panda, D. Ganguli, P. Mishra and S. Chaudhuri, *Cryst. Growth Des.*, 2007, **7**, 163.
25 K. Chang, Z. Wang, G. Huang, H. Li, W. Chen and J. Y. Lee, *J. Power Sources*, 2012, **201**, 259.

 